crystals

MDPI

Article

# $La_xPr_{4-x}Ni_3O_{10-\delta}$: Mixed A-Site Cation Higher-Order Ruddlesden-Popper Phase Materials as Intermediate-Temperature Solid Oxide Fuel Cell Cathodes

**Mudasir A. Yatoo [1,2], Zhihong Du [3], Zhang Yang [3], Hailei Zhao [3] and Stephen J. Skinner [1,2,*]**

1 Department of Materials, Faculty of Engineering, Imperial College London, Exhibition Road, London SW7 2AZ, UK; m.yatoo15@imperial.ac.uk
2 EPSRC Centre for Doctoral Training in Advanced Characterisation of Materials, Exhibition Road, London SW7 2AZ, UK
3 School of Materials Science and Engineering, University of Science and Technology Beijing, 30 Xueyuan Road, Haidian District, Beijing 100083, China; duzhihong1989@gmail.com (Z.D.); zhangyang_567@sina.com (Z.Y.); hlzhao@ustb.edu.cn (H.Z.)
* Correspondence: s.skinner@imperial.ac.uk

Received: 28 April 2020; Accepted: 22 May 2020; Published: 27 May 2020


**Abstract:** Systematic studies of the air electrode and full solid oxide fuel cell performance of $La_3PrNi_3O_{9.76}$, and $La_2Pr_2Ni_3O_{9.65}$ $n = 3$ Ruddlesden–Popper phases are reported. These phases were found to adopt orthorhombic symmetry with a decrease in lattice parameters on increasing Pr content, consistent with the solid solution series end members. From electrochemical impedance spectroscopy measurements of symmetrical cells, the electrodes were found to possess area specific resistances of 0.07 Ω $cm^2$ for the $La_2Pr_2Ni_3O_{9.65}$ cathode and 0.10 Ω $cm^2$ for the $La_3PrNi_3O_{9.76}$ cathode at 750 °C, representing a significant improvement on previously reported compositions. This significant improvement in performance is attributed to the optimisation of the electrode microstructure, introduction of an electrolyte interlayer and the resulting improved adhesion of the electrode layer. Following this development, the new electrode materials were tested for their single-cell performance, with the maximum power densities obtained for $La_2Pr_2Ni_3O_{9.65}$ and $La_3PrNi_3O_{9.76}$ being 390 mW $cm^{-2}$ and 400 mW $cm^{-2}$ at 800 °C, respectively. As these single-cell measurements were based on thick electrolytes, there is considerable scope to enhance over cell performance in future developments.

**Keywords:** solid oxide fuel cell; $La_xPr_{4-x}Ni_3O_{10-\delta}$; power density; impedance spectroscopy; microstructure

## 1. Introduction

Ruddlesden–Popper phases, with the general formula of $A_{n+1}B_nO_{3n+1}$, were first synthesised in 1958 [1]. The structure consists of $nABO_3$ perovskite layers which are sandwiched between two AO rock-salt layers [2]. This structural similarity of Ruddlesden–Popper (RP) phase materials to perovskites is one of the reasons behind the expectation of these materials working as solid oxide fuel cell (SOFC) cathodes. The anisotropic structural features of lower-order ($n = 1$) phases such as $La_2NiO_{4+\delta}$ (LNO) and $Pr_2NiO_{4+\delta}$ (PNO) permit them to accommodate a substantial amount of interstitial oxygen, which in turn leads to fast oxygen ion transport [3–11].

Lower-order RP phases have been studied extensively [4,12–16], with several studies focusing on the electrochemical performance of these materials [15–21]. Amow and Skinner obtained a relatively high area specific resistance (ASR) (>1.0 Ω $cm^2$ at 800 °C) [15,16], which was improved by Escudero

et al., who reported an ASR of 0.48 Ω $cm^2$ at 800 °C for LNO with a $La_{1-x}Sr_xGa_{1-y}Mg_yO_{3-\delta}$ (LSGM) electrolyte [18]. Aguadero et al. substituted the A site cation (La) and obtained their best performance of ASR = 3.7 Ω $cm^2$ at 850 °C for a Cu doped LNO [17]. As a further development, Rieu and Sayers reported graded LNO cathodes using a compact LNO interlayer between the electrolyte and the porous LNO cathode, which resulted in a seven-fold drop in ASR from 7.4 Ω $cm^2$ to 1.0 Ω $cm^2$ at 700 °C [19,21]. Each of these studies produced ASR values significantly above the target of <0.15 Ω $cm^2$, leading to further studies on the related Pr and Nd analogues. Initial studies of the $Pr_2NiO_{4+\delta}$ and $Nd_2NiO_{4+\delta}$ phases produced electrode performances with slightly higher ASRs; Ferchaud et al. reported an ASR of 2.5 Ω $cm^2$ for PNO at 600 °C [22]. A 50:50 composition, $PrNdNiO_{4+\delta}$ (PNNO), reported by Dogdibegovic et al., presented an ASR of 0.7 Ω $cm^2$ at 800 °C [23]. A recent attempt at improving the performance of these materials by Bassat et al. yielded the remarkable performance of 0.03 Ω $cm^2$ at 700 °C for a PNO cathode [24]. Building on this work, Vibhu and co-workers studied the mixed composition cathodes $La_{2-x}Pr_xNiO_{4+\delta}$ (LPNO) and were successful in improving the performance of half-cells, but they did note the problem of decomposition on increasing the Pr content of these mixed La and Pr cathodes [25].

The main problem, however, with the lower-order phases such as LNO, PNO and NNO is the phase stability of these materials under operating conditions, which effectively restricts the use of these materials as IT-SOFC cathodes [14–16,24–26]. Amow et al. studied cobalt doped LNO, $La_2Ni_{0.9}Co_{0.1}O_{4+\delta}$, and they observed extensive phase decomposition [26]. Vibhu and co-workers performed extensive ageing studies of PNO mixed nickelates, $Pr_{2-x}La_xNiO_{4+\delta}$ (LPNO), and reported severe decomposition of Pr rich phases in particular [25]. The impurity $Ni^{2+}/Ni^{3+}$ phase formation at 900 °C in LNO (and other $n$ = 1 Ruddlesden–Popper phase compositions) stems from the fact that stoichiometric $La_2NiO_{4+\delta}$ ($\delta$ = 0) is mainly comprised of $Ni^{2+}$ ions, while $Ni^{3+}$ is the predominant oxidation state in higher-order phases ($n$ = 2 and 3). Higher-order phases such as $La_4Ni_3O_{9.78}$ (L4N3) and $Pr_4Ni_3O_{10\pm\delta}$ (P4N3), comprising predominantly $Ni^{3+}$ ions, are expected to exhibit increased long-term stability. Indeed, Amow et al. did observe that higher-order phases showed increased stability and no impurity phase formation [16]. They reported the impurity phase formation after heating LNO at 900 °C for two weeks in air, while no such impurity was observed in the $n$ = 2 and 3 phases after ageing them at 900 °C for two weeks in air. Bassat et al. also studied and compared the stability and electrochemical behaviour of Pr-based Ruddlesden–Popper phases as cathodes for IT-SOFCs and observed the decomposition of PNO, whereas no such issue was observed in the studies of P4N3 [24]. Furthermore, higher-order Ruddlesden–Popper phases are known to exhibit higher total electrical conductivity than lower-order phases [14–16,27]. Recently, Berger et al. further developed this concept by substituting Co into the P4N3 composition [28] using a freeze-drying technique and identifying fast surface exchange coefficients and high total conductivity, but did not report any fuel cell performance or durability/stability data.

In light of the above discussion, this contribution details our recent studies of the $La_3PrNi_3O_{10-\delta}$ phase (L3P1N3) and $La_2Pr_2Ni_3O_{10-\delta}$ (L2P2N3), placing this in context with our earlier work on the $LaPr_3Ni_3O_{10\pm\delta}$ (L1P3N3) composition. Our recent report of impressive half-cell performance of the L1P3N3 composition [29], wherein the focus was on optimising the electrode microstructure and interface structure, forms the basis of this study. The lessons learned in our previous investigation of the L1P3N3 electrode have been implemented in studying the performance of the L3P1N3 and L2P2N3 phases. In addition, comparative X-ray diffraction studies and the single-cell testing performance of these compositions will be discussed.

## 2. Materials and Methods

### *2.1. Syntheses and Characterisation*

Both compositions (L3P1N3 and L2P2N3) were synthesised using the sol-gel route [30]. Stoichiometric amounts, depending on the material composition, of $La(NO_3)_3{\cdot}6H_2O$ (Sigma Aldrich,

99.0%), $Pr(NO_3)_3{\cdot}6H_2O$ (Sigma Aldrich, 99.99%) and $Ni(NO_3)_2{\cdot}6H_2O$ (Sigma Aldrich, 99.0%) were dissolved in an aqueous solution of 10% (by weight) of citric acid (Sigma Aldrich, 99.99%). The solution was heated at 250 °C, under constant stirring for three hours, until a gel was obtained. The gels, after being decomposed in air for 12 h at 600 °C, were ground in a mortar and pestle, and the resultant powder was further annealed for 24 h in air at 1000 °C prior to X-ray diffraction (XRD) analysis. The XRD patterns of the materials were collected using a PANalytical X'Pert Pro MPD (Cu $K_\alpha$ source, $\lambda$ = 1.5406 Å) and Rietveld refinement of the XRD data, performed with the GSAS/EXPGUI software package [31,32], which was used to confirm the phase identification and extract unit cell parameters. Post-test microstructural investigations were achieved using a LEO Gemini 1525 FEG scanning electron microscope with an accelerating voltage of 5.0 kV.

### 2.2. Cell Preparation

A commercially available $La_{0.8}Sr_{0.2}Ga_{0.8}Mg_{0.2}O_{3-\delta}$ (LSGM) electrolyte powder, purchased from Praxair Surface Technologies (Lot # 03-P6948DM), was pressed (0.04 MPa) into 13 mm diameter disks using a uniaxial press, followed by the cold isostatic press (300 MPa), and then sintered at 1450 °C for 8 h. The thickness of the LSGM pellets after sintering and polishing with silicon carbide paper (1200 grit) was in the 400–500 μm range. L3P1N3 and L2P2N3 electrode inks were prepared by mixing the as-prepared powders with an organic ink vehicle supplied by fuel cell materials (Lot # R1835, Item # 311006, USA) in a 2:1 weight ratio, and were used to prepare symmetrical cells using the screen-printing technique. After ball milling the electrode powders for 24 h, the electrode slurries were prepared by mixing the powders with the ink vehicle and triple roll milling the prepared ink to produce a slurry with a uniform particle size (~3 μm). A further ink consisting of only the electrolyte LSGM powder was prepared in a similar way to be used as an interlayer between the electrode and the LSGM pellet.

Symmetrical cells of the configuration L2P2N3|LSGMInk|LSGM|LSGMInk|L2P2N3 and L3P1N3|LSGMInk|LSGM|LSGMInk|L3P1N3 were prepared. Firstly, an LSGM interlayer ink was screen-printed on one face of the LSGM pellet, which was then dried for 10 min at 200 °C. An identical procedure was repeated for screen-printing the other face of the pellet, and this was later followed by annealing the cells for 1 h at 1000 °C. This was followed by screen-printing of the appropriate electrode layer ink on both sides of the samples, again drying the inks for 10 min at 200 °C at each step. All cells prepared had an active area of 0.5 $cm^2$. Two cells of each composition were prepared and sintered at two different temperatures; one sample of each composition, L2P2N3 (sample 1) and L3P1N3 (sample 2), were sintered at 1100 °C for 1 h. Since both the L2P2N3 and L3P1N3 compositions decompose at temperatures above 1050 °C, slow cooling (0.5 °C $min^{-1}$) to 950 °C from 1100 °C under an oxygen flow was required, which leads to the re-formation of the L2P2N3 and L3P1N3 higher-order phases. To make sure that the L2P2N3 and L3P1N3 compositions were fully recovered, the cells were maintained at 950 °C for 6 h. Another set of samples, L2P2N3 (sample 3) and L3P1N3 (sample 4), were sintered for 2.5 h at 1050 °C under an ambient atmosphere. The sample details are summarised in Table 1.

Pt mesh was used as a current collector for the electrochemical measurements. Impedance measurements of the symmetrical cells were performed using a Solartron 1260 impedance gain/phase analyser in combination with a Solartron 1287 electrochemical interface in the 0.1 to $10^6$ Hz frequency range with a perturbation amplitude of 10 mV.

**Table 1.** Summary of the cell preparation conditions for the six samples investigated.

| Sample | Composition | Electrode Sintering Conditions |
|---|---|---|
| 1 | L2P2N3 | 1150 °C/1 h, followed by cooling under air for 6 h |
| 2 | L3P1N3 | 1150 °C/1 h, followed by cooling under air for 6 h |
| 3 | L2P2N3 | 1050 °C/2.5 h, under ambient conditions |
| 4 | L3P1N3 | 1050 °C/2.5 h, under ambient conditions |

The cell configurations used for the single-cell performance measurements were NiO-GDC|LDC|LSGMPellet|LSGM Ink|Cathode Ink (where the cathode was L2P2N3 or L3P1N3). A LDC ($La_{0.4}Ce_{0.6}O_{1.8}$) buffer layer was used for interfacial stability between the anode and LSGM electrolyte [33]. The LSGM ink and LDC buffer layer were screen-printed onto the electrolyte pellets, and the cells were sintered for 1 h at 1000 °C. This was followed by screen-printing the cathode and anode and then sintering the complete cell at 1050 °C for 2.5 h. The current–power–voltage (IPV) curves were recorded in the range of 600–800 °C using a Solartron 1287 electrochemical interface controlled by CorrWare software, where the cell voltage was varied from OCV to 0.3 V. Humidified $H_2$ (~3% $H_2O$) was fed as fuel to the anode with a flow rate of 40 mL $min^{-1}$, with pure oxygen used as the oxidant at the cathode with a flow rate of 100 mL $min^{-1}$.

## 3. Results and Discussion

### *3.1. X-ray Diffraction*

Powder X-ray diffraction was used to initially characterise the synthesised cathode materials. It is well known that the Ruddlesden–Popper phases can adopt a variety of space group symmetries depending on the stoichiometry of the material. To fully evaluate the crystal chemistry of these new materials, three space groups, orthorhombic *Bmab*, orthorhombic *Fmmm* and monoclinic $P2_1/a$, as previously proposed, were evaluated [27,34,35] for both of the prepared compositions. The XRD characterisation, followed by Rietveld refinement of L3P1N3, concluded that this material crystallised with an orthorhombic structure adopting the *Fmmm* space group (Figure 1). It should be noted that the oxygen content was fixed to full stoichiometry for the refinement, i.e., all oxygen positions had an occupancy of 1 corresponding to the $La_3PrNi_3O_{10}$ composition. This was necessary as refining oxygen content from XRD data is inherently unreliable. Similarly, XRD data collected previously for the L2P2N3 and L1P3N3 compositions [29,36] were refined in the orthorhombic *Fmmm* and monoclinic $P2_1/a$ space groups, respectively.

The lattice parameters for L3P1N3 were determined to be $a$ = 5.406(1) Å, $b$ = 5.466(1) Å and $c$ = 27.873(9) Å, and are in close agreement with the previously reported results for the end member materials [27,37]. The lattice parameters of the L2P2N3 and L1P3N3 compositions, obtained through the application of Rietveld refinement previously reported by the authors, are shown in Table 2. The lattice parameters, when compared to the two end members, $La_4Ni_3O_{9.78}$ and $Pr_4Ni_3O_{10.10}$, show a smooth decrease with increasing Pr content (Table 2), which is consistent with the variation of the ionic radius [38], leading to an overall decrease in the cell volume. This is not surprising and is attributed to the ionic radius of the $Pr^{3+}$ ion (1.179 Å) being smaller than $La^{3+}$ (1.216Å) in 9-fold coordination [38].

**Table 2.** Unit-cell parameter comparison of the prepared compositions of L2P2N3 and L3P1N3. The two end members, L4N3 and P4N3, are also included to show the systematic decrease of lattice parameters with increasing Pr content, which is consistent with the variation of the ionic radii, leading to an overall decrease in the cell volume with increasing Pr content. Note the data for L2P2N3 are from reference 35.

| Composition | a(Å) | b(Å) | c(Å) | β(°) | Space Group | Ref. |
|---|---|---|---|---|---|---|
| $La_4Ni_3O_{10-\delta}$ | 5.415(1) | 5.465(1) | 27.959(9) | 90 | *Fmmm* | [27] |
| $La_3PrNi_3O_{10-\delta}$ | 5.406(1) | 5.466(1) | 27.873(9) | 90 | *Fmmm* | This work |
| $La_2Pr_2Ni_3O_{10-\delta}$ | 5.392(3) | 5.465(3) | 27.7901(2) | 90 | *Fmmm* | [36] |
| $LaPr_3Ni_3O_{10-\delta}$ | 5.383(2) | 5.463(2) | 27.676(2) | 90.280(4) | $P2_1/a$ | [29] |
| $Pr_4Ni_3O_{10.10}$ | 5.3714(2) | 5.4611(2) | 27.5271(3) | 90 | *Fmmm* | [39] |

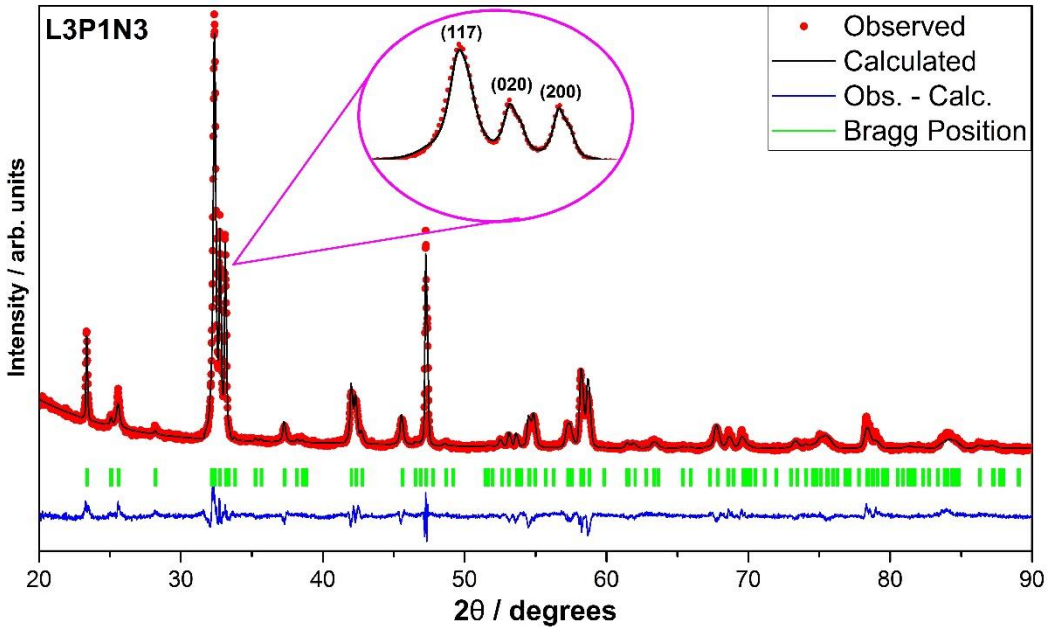


**Figure 1.** Rietveld refinement of the X-ray diffraction pattern of $La_3PrNi_3O_{9.76}$ using the orthorhombic Fmmm space group ($\chi^2$ = 4.2, $R_p$ 4.6%, $R_{wp}$ = 6.5%).

### *3.2. Symmetrical Cell Performance Testing*

LSGM was selected as the electrolyte for cell testing because of its good low-temperature electrolyte properties [40] and its reported superior performance and chemical compatibility with Ruddlesden–Popper phases [14,41,42]. The cathode performance of the L2P2N3 (samples 1 and 3) and L3P1N3 (samples 2 and 4) compositions was initially investigated using impedance spectroscopy to determine the area specific resistance (ASR) of the materials. Typical Nyquist plots and fitting results with equivalent circuit LR($CPE_1R_1$), where L is the inductance, R represents the ohmic resistance and ($CPE_1R_1$) represents the constant phase element and resistance of the electrode process, are shown in Figure 2.

In all samples, the total resistance decreased with increasing temperature, as expected, indicating the thermal behaviour of the electrode reaction processes. The ASR values obtained for the L2P2N3 electrode were 0.15 Ω $cm^2$ and 0.07 Ω $cm^2$ at 750 °C for samples 1 and 3, respectively. This contrasts dramatically with our earlier results, where a higher ASR—0.56 Ω $cm^2$ at 750 °C—was reported [36]. Our optimisation procedure, consisting of ball milling the initial electrode and using a LSGM interlayer, evidently improved the overall electrode performance. The corresponding ASR values for the L3P1N3 electrode were 0.17 Ω $cm^2$ and 0.10 Ω $cm^2$ at 750 °C for samples 2 and 4, respectively. One clear observation is that sintering of the electrode for a shortened period of time (2.5 h (samples 3, 4)) under

an ambient atmosphere presents a lower ASR than the corresponding ASR obtained for the same electrode sintered under an oxygen atmosphere followed by slow cooling (samples 1, 2). One possible reason for this observation could be the elongated periods of time (11–14 h) required for the cell sintering procedure under an oxygen atmosphere because the overall process involves sintering at a lower temperature (950 °C for 6 h) to allow for the reformation of the $n$ = 3 Ruddlesden–Popper phase. This was not the case with ambient atmosphere sintering of the electrode, used for preparing samples 2 and 4.

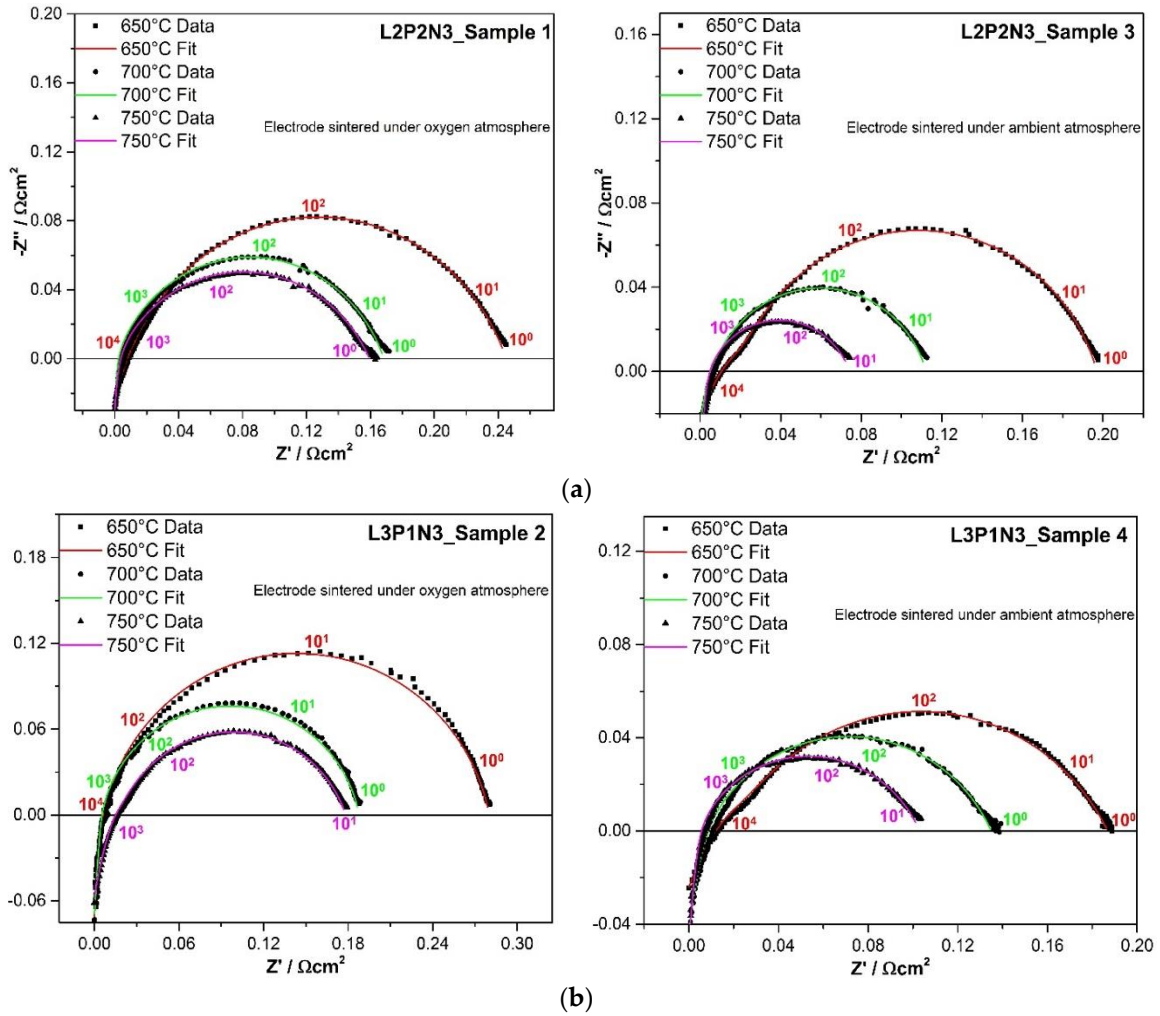


**Figure 2.** Nyquist plots recorded for samples (**a**) 1 and 3 (L2P2N3) and (**b**) 2 and 4 (L3P1N3). Samples 1 and 2, sintered under an oxygen atmosphere followed by slow heating, present higher corresponding area specific resistances (ASRs) than samples 3 and 4 sintered under an ambient atmosphere.

To put the results obtained in perspective, Table 3 shows the resistances obtained at different temperatures for the L3P1N3 electrode (samples 2 and 4) and L2P2N3 electrode (samples 1 and 3). It is evident from the data in Table 3, and from previous studies [29], that the calculated ASR values decrease with the increase of Pr content (25% in the L3P1N3 composition to 75% in the L1P3N3 composition [29]). A similar finding was reported for the $n$ = 1 RP phase ($La_{2-x}Pr_xNiO_{4+\delta}$) by Vibhu et al. [25], wherein they reported that electrode performance increased with an increase in the Pr content of a composition. This was ascribed to improved catalytic properties of Pr as compared to La.

**Table 3.** Systematic improvement in half-cell performance on increasing Pr content across different compositions and improvement in ASR performance within a composition by reducing the effective cell sintering time.

| – | L3P1N3 Electrode ASR | | L2P2N3 Electrode ASR | |
|---|---|---|---|---|
| | **Sample 2** | **Sample 4** | **Sample 1** | **Sample 3** |
| **650 °C** | 0.28 Ω $cm^2$ | 0.20 Ω $cm^2$ | 0.24 Ω $cm^2$ | 0.19 Ω $cm^2$ |
| **700 °C** | 0.19 Ω $cm^2$ | 0.14 Ω $cm^2$ | 0.17 Ω $cm^2$ | 0.11 Ω $cm^2$ |
| **750 °C** | 0.17 Ω $cm^2$ | 0.10 Ω $cm^2$ | 0.15 Ω $cm^2$ | 0.07 Ω $cm^2$ |

### 3.3. Single Button Cell Testing

Single-cells of each composition were tested under open circuit conditions (OCV) with a measured OCV of 1.10 V, which agrees well with the theoretical value calculated from the Nernst equation, thereby indicating minimum gas leakage. The maximum power densities (MPD) obtained over a range of temperatures for both compositions are outlined in Figure 3 and summarised below in Table 4.

**Table 4.** Maximum power densities obtained from single-cell measurements using the L2P2N3 and L3P1N3 cathodes as a function of measurement temperature.

| | **Maximum Power Density/mWcm$^{-2}$** | | | | |
|---|---|---|---|---|---|
| **Sample** | **800 °C** | **750 °C** | **700 °C** | **650 °C** | **600 °C** |
| **L2P2N3** | 390 | 310 | 230 | 160 | 100 |
| **L3P1N3** | 400 | 325 | 250 | 180 | 120 |

The highest MPD was obtained for the L3P1N3 composition, 400 mW $cm^{-2}$ at 800 °C. It should be noted that in each case, the cells were based on relatively thick (~400 µm) electrolytes which could be thinned to minimise the Ohmic losses and thus achieve higher power densities. We also noted that there was a small difference between the minimum ASRs obtained and the maximum power densities. This is ascribed to small differences in the electrolyte and electrode layer thicknesses, as shown in the subsequent section. It was noted that the post-test XRD (not shown) found all of the material compositions retained their structural integrity and that there was no discernible phase evolution of the electrode.

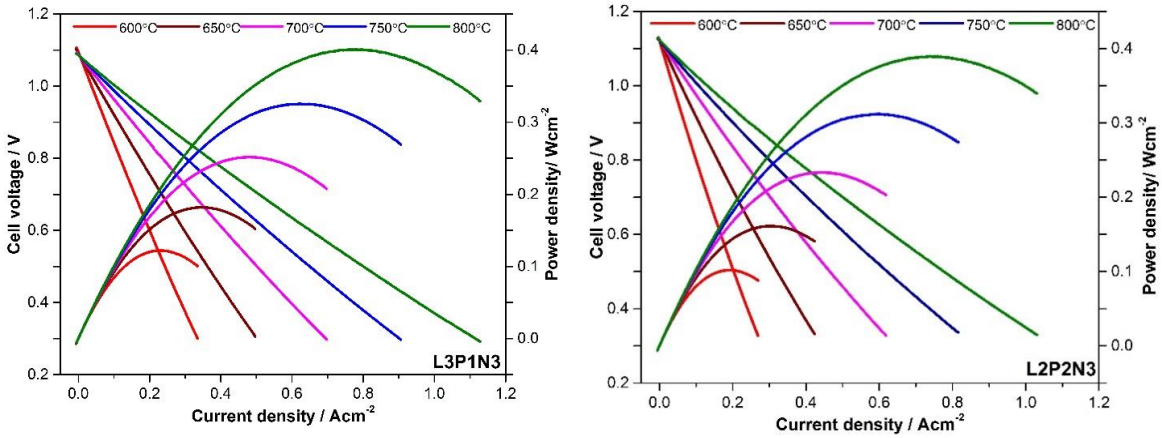


**Figure 3.** IPV curves obtained for single-cell measurements of the L3P1N3 and L2P2N3 based cells with humidified (3% $H_2O$) pure hydrogen as a fuel and pure oxygen as the oxidant, highlighting the overall maximum power densities reaching 0.4 W $cm^{-2}$ at 800 °C.

### *3.4. Post-Test Microstructural Studies*

#### 3.4.1. Symmetrical Cells

The secondary electron SEM images—in both the top view and cross-section view of the electrode layer and cell, respectively—obtained for the L2P2N3 electrode (samples 1 and 3) and L3P1N3 electrode (samples 2 and 4) after symmetrical-cell testing are presented in Figure 4; Figure 5.

Figure 4 illustrates the post-test microstructural SEM images of samples 1 and 2, i.e., those sintered at 1150 °C with subsequent annealing at 950 °C for 6 h in oxygen. It is clear from these images that the electrode/interlayer and interlayer/electrolyte interfaces are well adhered, in contrast to the data previously reported for the L2P2N3 composition [36]. This highlights the significant improvement in the cell preparation methods developed. In addition, these microstructural data correlate well with the cathode performance determined by impedance spectroscopy measurements. As mentioned previously, the ASR of the L2P2N3 electrodes decreased from 0.56 Ω $cm^2$ (reported previously [36]) to 0.15 Ω $cm^2$ at a measurement temperature of 750 °C, which is ascribed to the ball milling of the electrode material and introduction of an LSGM buffer layer. A further reduction in the ASR from 0.15 Ω $cm^2$ to 0.07 Ω $cm^2$ at 750 °C is attributed to the reduction of the effective cell sintering time, of which the direct impact is negligible particle coarsening (Figure 5). Similar behaviour is observed in the L3P1N3 composition; sample 2 in Figure 4 shows mild particle coarsening and sintering (~5 µm) compared to sample 4, which shows almost no particle coarsening (Figure 5). This is also attributed to the reduction of the electrode sintering time, and this is also reflected in the half-cell performance of L3P1N3, with samples 2 and 4 presenting ASR values of 0.17 Ω $cm^2$ and 0.10 Ω $cm^2$ at 750 °C, respectively.

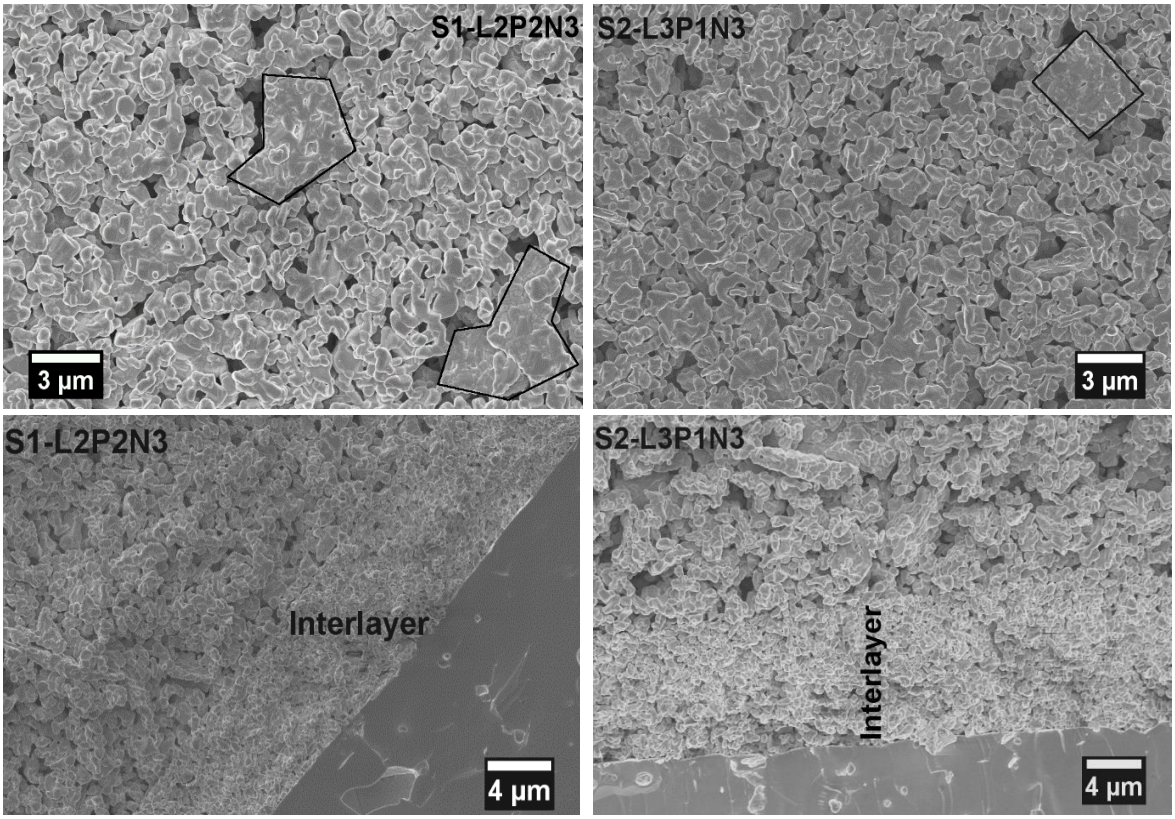


**Figure 4.** Post-test microstructural secondary electron SEM images showing the top view (TV) and cross-section (CS) view of the electrode in left: sample 1 (L2P2N3 electrode) and right: sample 2 (L3P1N3). Ball milling and triple roll milling improves the microstructure, but slight coarsening and sintering (highlighted areas) of the electrode in these samples can be observed. The use of an interlayer prepared from a LSGM electrolyte powder allows the interface to adhere strongly.

The introduction of the buffer layer shows a clear impact by increasing the number of contact points at the electrode/electrolyte interface, which ultimately decreases the interface polarisation resistance contribution. Furthermore, as illustrated in Figure 5, SEM images of samples 3 and 4 taken at high magnification show excellent particle interconnectivity, and the cathodes present porous structures. This interconnectivity of the electrode particles and the porous structure of the cathode are expected to facilitate oxygen transport by providing an extended network of active pathways for oxygen diffusion and charge transfer.

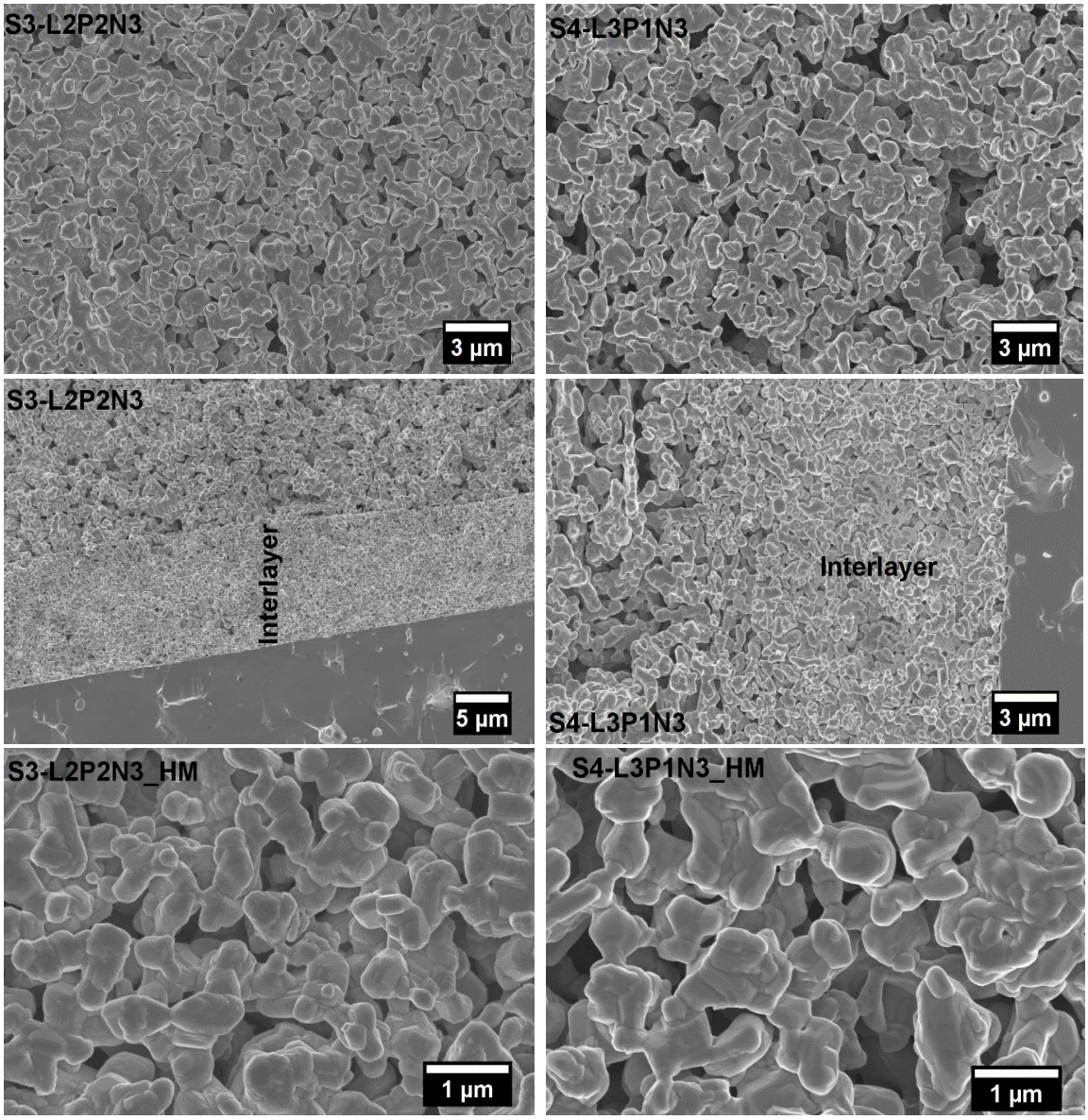


**Figure 5.** Post-test microstructural secondary electron SEM images showing the TV and CS view of the electrode in sample 3 (L2P2N3) and sample 4 (L3P1N3). The cross-section view shows strong adherence of the electrode layer, as was observed in samples 1 and 2. Top-view SEM images show virtually no particle coarsening in samples 3 and 4. The high-magnification (HM) images further illustrate the improved particle interconnectivity and porous cathode structure.

### 3.4.2. Single Fuel Cell Microstructure Analysis

Post-test single-cell microstructural studies showed similar results, as discussed in the previous section, for the symmetrical half-cells. The SEM images illustrated in Figure 6 highlight the

microstructure and interface adherence in post-test single-cells based on L2P2N3 and L3P1N3 cathodes. The images demonstrate that a porous cathode structure with considerable particle interconnectivity is maintained through the cell test, although minor particle coarsening/sintering was observed, in contrast to the half-cells measured at OCV. The electrode screen-printed over the electrolyte interface layer, as observed in the previous section, shows strong adhesion.

It is pertinent here to point out that there are some discernible differences between the post-test microstructure obtained after half- and single-cell testing that could be the reason behind the anomalous half- and single-cell behaviour described in the previous section. The interlayer appears denser in the prepared single-cells and the electrode is significantly more porous when compared to the half-cells. The thickness of the interlayer varies slightly, with L2P2N3 and L3P1N3 single-cells showing a thickness of ~8 µm, while all the half-cells are slightly thicker at around 10 µm. Irrespective of these slight variations, it is clear that the introduction of an electrolyte interlayer has a significant positive effect on the adhesion, and thus performance of $La_{4-x}Pr_xNi_3O_{10+/-\delta}$ electrodes for solid oxide fuel cells.

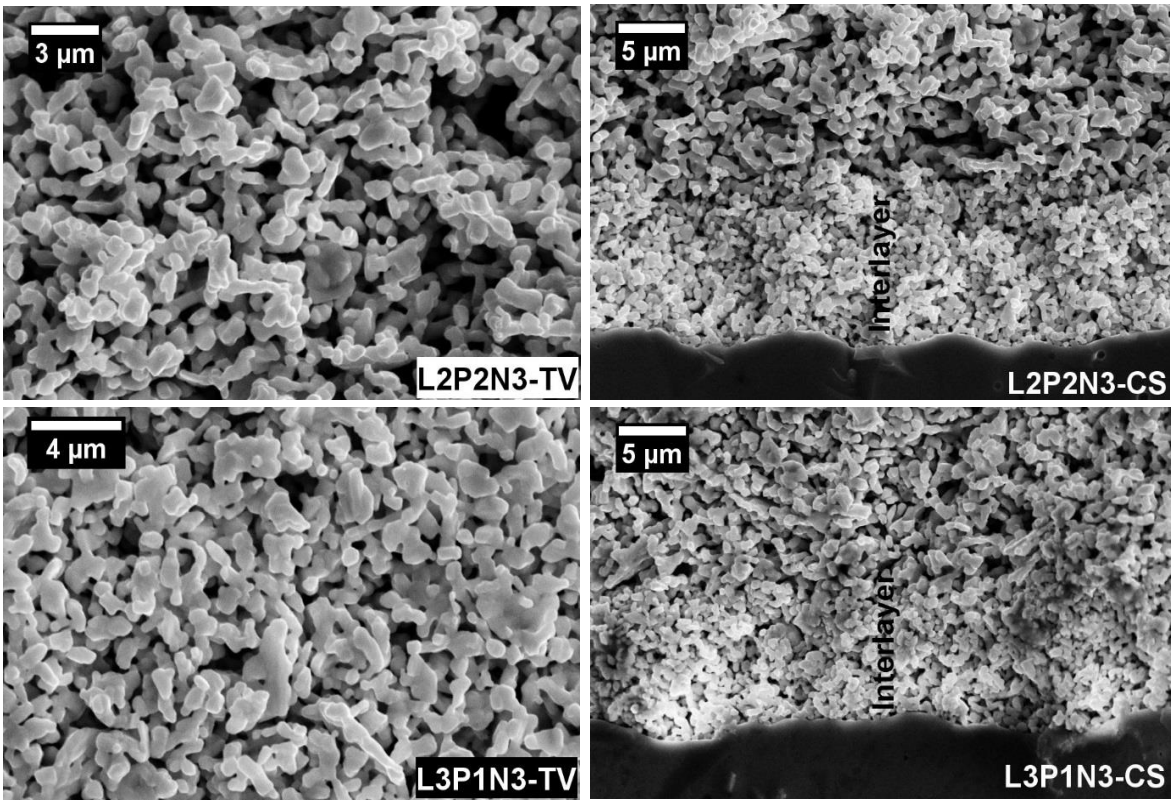


**Figure 6.** Post-test SEM images of single fuel cells based on L2P2N3 and L3P2N3 cathodes showing a porous cathode structure, with minor particle coarsening. The interface structure retains the integrity observed in half-cell samples.

## 4. Conclusions

Two higher-order Ruddlesden–Popper phase materials were investigated for IT-SOFC cathode applications. The materials, L2P2N3 and L3P1N3, were synthesised by a sol-gel method and were later characterised by X-ray powder diffraction. Lattice parameters showed a systematic decrease with increasing Pr content, which is in agreement with the concept of effective ionic radii being the main driver of this observation; the ionic radius of Pr is lower than La [27,38] in equivalent coordination environments.

The best half-cell performance of 0.07 Ω $cm^2$ and 0.10 Ω $cm^2$, respectively, for a L2P2N3 and L3P1N3 electrode operating at 750 °C was obtained, which fits in well with our previous report of 0.05 Ω $cm^2$ at 750 °C for a L1P3N3 electrode. This is the first report showing such low ASR values for

$n$ = 3 Ruddlesden–Popper compositions with LSGM electrolytes, and offers opportunities to develop a new series of high-performance devices. All of these electrodes in half-cell configurations exceeded the requirement of <0.15 Ω $cm^2$ at 700 °C, and with further optimisation, will have applications in the low operating temperature regime (<600 °C).

Testing of single-cells revealed maximum power densities for the L2P2N3 and L3P1N3 compositions of 390 mW $cm^{-2}$ and 400 mW $cm^{-2}$ at 800 °C, respectively, highlighting a marginally higher performance at a lower Pr content. Post-test microstructural analysis after both half- and single-cell testing revealed that the cathode microstructure was porous with considerable particle interconnectivity. It was observed that the use of a buffer layer of LSGM between the electrode and LSGM electrolyte significantly improved the contact and is suggested to be the driver for the performance improvement in these materials.

**Author Contributions:** The work was conceived of and supervised by S.J.S. M.A.Y. performed all of the synthesis, structural, microstructural, electrochemical measurements and data analysis. M.A.Y. wrote the manuscript draft which was revised by S.J.S., and H.Z. Full fuel cell measurements were performed by M.A.Y., Z.D., and Z.Y. under the local supervision of H.Z. S.J.S., and M.A.Y. discussed the data analysis and interpretation. All authors have read and agreed to the published version of the manuscript.

**Funding:** This research was funded through the award of an Imperial College London President's Ph.D. Scholarship to M.A.Y. The APC was funded by Imperial College London Library Open Access Fund.

**Acknowledgments:** The authors would like to thank the Imperial College President's PhD Scholarships and EPSRC Centre for Doctoral Training in the Advanced Characterisation of Materials (EP/L015277/1) for funding this research.

**Conflicts of Interest:** The authors declare no conflict of interests.

## References

1. Ruddlesden, S.N.; Popper, P. The Compound $Sr_3Ti_2O_7$ and its structure. *Acta Cryst.* **1958**, *11*, 54–55. [CrossRef]
2. Beznosikov, B.V.; Aleksandrov, K.S. Perovskite-like crystals of the Ruddlesden-Popper series. *Crystallogr. Rep.* **2000**, *45*, 792–798. [CrossRef]
3. Kharton, V.V.; Viskup, A.P.; Kovalevsky, A.V.; Naumovich, E.N.; Marques, F.M.B. Ionic transport in oxygen-hyperstoichiometric phases with $K_2NiF_4$-type structure. *Solid State Ionics* **2001**, *143*, 337–353. [CrossRef]
4. Kharton, V.V.; Viskup, A.P.; Naumovich, E.N.; Marques, F.M.B. Oxygen ion transport in $La_2NiO_4$-based ceramics. *J. Mater. Chem.* **1999**, *9*, 2623–2629. [CrossRef]
5. Skinner, S.J. Characterisation of $La_2NiO_{4+\delta}$ using in-situ high temperature neutron powder diffraction. *Solid State Sci.* **2003**, *5*, 419–426. [CrossRef]
6. Demourgues, A.; Wattiaux, A.; Grenier, J.C.; Pouchard, M.; Soubeyroux, J.L.; Dance, J.M.; Hagenmuller, P. Electrochemical Preparation and Structural Characterization of $La_2NiO_{4+\delta}$ Phases ($0 \leq \delta \leq 0.25$). *J. Solid State Chem.* **1993**, *105*, 458–468. [CrossRef]
7. Paulus, W.; Cousson, A.; Dhalenne, G.; Berthon, J.; Revcolevschi, A.; Hosoya, S.; Treutmann, W.; Heger, G.; Le Toquin, R. Neutron diffraction studies of stoichiometric and oxygen intercalated La2NiO4 single crystals. *Solid State Sci.* **2002**, *4*, 565–573. [CrossRef]
8. Read, M.S.D.; Islam, M.S.; Watson, G.W.; Hancock, F.E. Surface structures and defect properties of pure and doped $La_2NiO_4$. *J. Mater. Chem.* **2001**, *11*, 2597–2602. [CrossRef]
9. Minervini, L.; Grimes, R.W.; Kilner, J.A.; Sickafus, K.E. Oxygen migration in $La_2NiO_{4+\delta}$. *J. Mater. Chem.* **2000**, *10*, 2349–2354. [CrossRef]
10. Frayret, C.; Villesuzanne, A.; Pouchard, M. Application of Density Functional Theory to the Modeling of the Mixed Ionic and Electronic Conductor $La_2NiO_{4+\delta}$: Lattice Relaxation, Oxygen Mobility, and Energetics of Frenkel Defects. *Chem. Mater.* **2005**, *17*, 6538–6544. [CrossRef]
11. Yan, L.; Niu, H.J.; Duong, G.V.; Suchomel, M.R.; Bacsa, J.; Chalker, P.R.; Hadermann, J.; van Tendeloo, G.; Rosseinsky, M.J. Cation ordering within the perovskite block of a six-layer Ruddlesden-Popper oxide from layer-by-layer growth—Artificial interfaces in complex unit cells. *Chem. Sci.* **2011**, *2*, 261–272. [CrossRef]
12. Skinner, S.J.; Kilner, J.A. Oxygen diffusion and surface exchange in $La_{2-x}Sr_xNiO_{4+\delta}$. *Solid State Ionics* **2000**, *135*, 709–712. [CrossRef]

13. Boehm, E.; Bassat, J.M.; Dordor, P.; Mauvy, F.; Grenier, J.C.; Stevens, P. Oxygen diffusion and transport properties in non-stoichiometric $Ln_{2-x}NiO_{4+\delta}$ oxides. *Solid State Ionics* **2005**, *176*, 2717–2725. [CrossRef]
14. Amow, G.; Skinner, S.J. Recent developments in Ruddlesden–Popper nickelate systems for solid oxide fuel cell cathodes. *J. Solid State Electrochem.* **2006**, *10*, 538–546. [CrossRef]
15. Amow, G.; Davidson, I. Preliminary investigation of the higher order Ruddlesden-Popper phases for IT-SOFC cathodes, $La_{n+1}Ni_nO_{3n+1}$ (n=2 and 3). *Proc. Electrochem. Soc.* **2005**, *PV 2005-07*, 1745–1750. [CrossRef]
16. Amow, G.; Davidson, I.; Skinner, S.J. A comparative study of the Ruddlesden-Popper series, $La_{n+1}Ni_nO_{3n+1}$ (n = 1, 2 and 3), for solid-oxide fuel-cell cathode applications. *Solid State Ionics* **2006**, *177*, 1205–1210. [CrossRef]
17. Aguadero, A.; Alonso, J.A.; Escudero, M.J.; Daza, L. Evaluation of the $La_2Ni_{1-x}Cu_xO_{4+\delta}$ system as SOFC cathode material with 8YSZ and LSGM as electrolytes. *Solid State Ionics* **2008**, *179*, 393–400. [CrossRef]
18. Escudero, M.J.; Fuerte, A.; Daza, L. $La_2NiO_{4+\delta}$ potential cathode material on $La_{0.9}Sr_{0.1}Ga_{0.8}Mg_{0.2}O_{2.85}$ electrolyte for intermediate temperature solid oxide fuel cell. *J. Power Sources* **2011**, *196*, 7245–7250. [CrossRef]
19. Rieu, M.; Sayers, R.; Laguna-Bercero, M.A.; Skinner, S.J.; Lenormand, P.; Ansart, F. Investigation of graded $La_2NiO_{4+d}$ cathodes to improve SOFC electrochemical performance. *J. Electrochem. Soc.* **2010**, *157*, B477–B480. [CrossRef]
20. Sayers, R.; Liu, J.; Rustumji, B.; Skinner, S.J. Novel $K_2NiF_4$-Type Materials for Solid Oxide Fuel Cells: Compatibility with Electrolytes in the Intermediate Temperature Range. *Fuel Cells* **2008**, *8*, 338–343. [CrossRef]
21. Sayers, R.; Rieu, M.; Lenormand, P.; Ansart, F.; Kilner, J.A.; Skinner, S.J. Development of lanthanum nickelate as a cathode for use in intermediate temperature solid oxide fuel cells. *Solid State Ionics* **2011**, *192*, 531–534. [CrossRef]
22. Ferchaud, C.; Grenier, J.-C.; Zhang-Steenwinkel, Y.; van Tuel, M.M.A.; van Berkel, F.P.F.; Bassat, J.-M. High performance praseodymium nickelate oxide cathode for low temperature solid oxide fuel cell. *J. Power Sources* **2011**, *196*, 1872–1879. [CrossRef]
23. Dogdibegovic, E.; Yan, J.; Cai, Q.; Jung, H.Y.; Xing, Z.; Liu, Z.; Goettler, R.W.; Zhou, X.-D. Activity and Stability of $(Pr_{1-x}Nd_x)_2NiO_{4+\delta}$ as Cathodes for Oxide Fuel Cells: Part VI. The Role of Cu Dopant on the Structure and Electrochemical Properties. *J. Electrochem. Soc.* **2017**, *164*, F3131–F3139. [CrossRef]
24. Bassat, J.-M.; Vibhu, V.; Nicollet, C.; Flura, A.; Fourcade, S.; Grenier, J.-C.; Rougier, A. Comparison of Pr-Based Cathodes for IT-SOFCs in the Ruddlesden-Popper Family. *ECS Trans.* **2017**, *78*, 655–665. [CrossRef]
25. Vibhu, V.; Bassat, J.-M.; Flura, A.; Nicollet, C.; Grenier, J.-C.; Rougier, A. Influence of La/Pr Ratio on the Ageing Properties of $La_{2-x}Pr_xNiO_{4+\delta}$ as cathodes in IT-SOFCs. *ECS Trans.* **2015**, *68*, 825–835. [CrossRef]
26. Amow, G.; Whitfield, P.S.; Davidson, I.J.; Hammond, R.P.; Munnings, C.N.; Skinner, S.J. Structural and sintering characteristics of the $La_2Ni_{1-x}Co_xO_{4+\delta}$ series. *Ceram. Inter.* **2004**, *30*, 1635–1639. [CrossRef]
27. Zhang, Z.; Greenblatt, M. Synthesis, structure, and properties of $Ln_4Ni_3O_{10-\delta}$ (Ln= La, Pr, and Nd). *J. Solid State Chem.* **1995**, *117*, 236–246. [CrossRef]
28. Berger, C.; Bucher, E.; Egger, A.; Schrodl, N.; Lammer, J.; Gspan, C.; Merkle, R.; Grogger, W.; Maier, J.; Sitte, W. Oxygen surface exchange kinetics and electronic conductivity of the third-order Ruddlesden-Popper phase $Pr_4Ni_{2.7}Co_{0.3}O_{10-d}$. *Solid State Ionics* **2020**, *348*, 115282. [CrossRef]
29. Yatoo, M.A.; Aguadero, A.; Skinner, S.J. $LaPr_3Ni_3O_{9.76}$ as a candidate solid oxide fuel cell cathode: Role of microstructure and interface structure on electrochemical performance. *APL Mater.* **2019**, *7*, 013204. [CrossRef]
30. Pechini, M.P. Method of Preparing Lead and Alkaline Earth Titanates and Niobates and Coating Method Using the Same to form a Capacitor. U.S. Patent 3,330,697, 11 July 1967.
31. Toby, B. EXPGUI, a graphical user interface for GSAS. *J. Appl. Cryst.* **2001**, *34*, 210–213. [CrossRef]
32. Larson, A.C.; Von Dreele, R.B. *General Structure Analysis System (GSAS) Los Alamos National Laboratory Report LAUR*; Los Almos National Laboratory: Los Almos, NM, USA, 2004; pp. 86–748.
33. Hong, J.-E.; Ida, S.; Ishihara, T. Effects of transition metal addition on sintering and electrical conductivity of La-doped $CeO_2$ as buffer layer for doped $LaGaO_3$ electrolyte film. *Solid State Ionics* **2014**, *262*, 374–377. [CrossRef]
34. Ling, C.D.; Argyriou, D.N.; Wu, G.; Neumeier, J.J. Neutron Diffraction Study of $La_3Ni_2O_7$: Structural Relationships among n=1, 2, and 3 Phases $La_{n+1}Ni_nO_{3n+1}$. *J. Solid State Chem.* **2000**, *152*, 517–525. [CrossRef]
35. Olafsen, A.; Fjellvåg, H.; Hauback, B.C. Crystal structure and properties of $Nd_4Co_3O_{10+\delta}$ and $Nd_4Ni_3O_{10+\delta}$. *J. Solid State Chem.* **2000**, *151*, 46–55. [CrossRef]

36. Yatoo, M.A.; Du, Z.; Zhao, H.; Aguadero, A.; Skinner, S.J. $La_2Pr_2Ni_3O_{10\pm\delta}$ Ruddlesden-Popper phase as potential intermediate temperature-solid oxide fuel cell cathodes. *Solid State Ionics* **2018**, *320*, 148–151. [CrossRef]
37. Bassat, J.M.; Allancon, C.; Odier, P.; Loup, J.P. Electronic properties of $Pr_4Ni_3O_{10\pm\delta}$. *Eur. J. Solid State Lnorg. Chem.* **1998**, *35*, 173–188. [CrossRef]
38. Shannon, R. Revised effective ionic radii and systematic studies of interatomic distances in halides and chalcogenides. *Acta Crystallogr. A* **1976**, *32*, 751–767. [CrossRef]
39. Vibhu, V.; Rougier, A.; Nicollet, C.; Flura, A.; Fourcade, S.; Penin, N.; Grenier, J.-C.; Bassat, J.-M. $Pr_4Ni_3O_{10+\delta}$: A new promising oxygen electrode material for solid oxide fuel cells. *J. Power Sources* **2016**, *317*, 184–193. [CrossRef]
40. Ishihara, T.; Shibayama, T.; Honda, M.; Nishiguchi, H.; Takita, Y. Intermediate temperature solid oxide fuel cells using $LaGaO_3$ electrolyte II. Improvement of oxide ion conductivity and power density by doping Fe for Ga site of $LaGaO_3$. *J. Electrochem. Soc.* **2000**, *147*, 1332–1337. [CrossRef]
41. Woolley, R.J. Ruddlesden-Popper Phases as Solid Oxide Fuel Cell Cathodes: Electrochemical Performance and In Situ Characterisation. Ph.D. Thesis, Imperial College London, London, UK, 2013.
42. Woolley, R.J.; Skinner, S.J. Novel $La_2NiO_{4+delta}$ and $La_4Ni_3O_{10\text{-}delta}$ composites for solid oxide fuel cell cathodes. *J. Power Sources* **2013**, *243*, 790–795. [CrossRef]